Small signal model of modular multilevel matrix converter for fractional frequency transmission system

Luo, Jiajie; Zhang, Xiao-ping; Xue, Ying

DOI:
10.1109/ACCESS.2019.2932050

This article has been accepted for publication in a future issue of this journal, but has not been fully edited. Content may change prior to final publication. Citation information: DOI 10.1109/ACCESS.2019.2932050, IEEE Access

Small Signal Model of Modular Multilevel Matrix Converter for Fractional Frequency Transmission System

JIAJIE LUO, XIAO-PING ZHANG (Senior Member, IEEE) AND YING XUE (Member, IEEE)

Department of Electronic, Electrical and Systems Engineering, University of Birmingham, Birmingham B15 2TT, U.K.

Corresponding author: Xiao-Ping Zhang (x.p.zhang@bham.ac.uk)

ABSTRACT Fractional frequency transmission is a promising technology for medium distance offshore wind power transmission. The key component in the fractional frequency transmission system (FFTS) is the modular multilevel matrix converter (M^3C). It is regarded as the next generation AC/AC converter for high voltage and high power applications due to various advantages such as high-quality waveforms, scalability and controllability. It is important to fully study its impact on the power network. The key to the understanding and impact is the development of a suitable model, which is the focus of this paper. A small signal model of the M^3C taking into account the dynamics of the capacitor voltage, AC currents and the control system is developed. Electrical quantities from both AC sides at different frequencies couple in the M^3C since there is no DC link. The complicated nonlinear terms in ABC frame are isolated and transformed in DQ frame. The model is convenient to interface with the control system and external AC systems. Small signal analysis is carried out on the influence of the controller parameters and sub-module capacitance. The correctness of the proposed model is verified by comparing to a detailed electromagnetic transient model of the M^3C simulated in RTDS.

INDEX TERMS Fractional frequency transmission system, small signal model, modular multilevel matrix converter, AC/AC converter, energy storage.

I. INTRODUCTION

Offshore wind power develops rapidly in recent years. Its penetration keeps growing and the market witnesses increasing investments and decrease of product prices [1]. Away from the population center, offshore wind is advantageous not only because of not taking up city land, but also due to higher wind speed and suitability for large-scale exploitation. Traditional high voltage AC (HVAC) is not capable of long distance offshore transmission [2], while fractional frequency transmission (FFT) proposed in [3] is able to overcome its cable shortcoming and it is an economical solution for medium distance offshore wind power transmission [4]. The principle is to use a proportion of the system frequency, mostly 1/3, for the offshore system. Compared to high voltage DC (HVDC) transmission, another merit of FFT is the offshore grid forming capability, as AC technology is well developed and it is more reliable especially with a high penetration level of offshore wind power in the future.

The core component of a FFTS is the frequency changer, or the AC/AC converter. In early research, cycloconverter was often adopted since it has been used in driving applications [5]. However, it is not an ideal candidate for offshore wind connection. Because the grid code has stringent requirements on fault ride through capability and harmonics level of wind power conversion and transmission systems, but cycloconverter has poor controllability and heavy harmonics [6]. On the contrary, modular multilevel matrix converter (M^3C) enjoys advantages including low loss and harmonics, full controllability and flexible scalability, making it particularly suitable for high voltage applications, e.g., offshore wind power transmission [7].

First introduced in 2001 [8], M^3C has been proposed for various applications, mainly in wind power integration [9, 10] and motor driving [11, 12], and also in power quality enhancement as a unified power quality conditioner (UPQC) [13]. In [11], a decoupled current control method was proposed for M^3C on medium voltage motor drives. A three-phase 400V 15kW experiment system was developed to verify the performance. [12] focused on optimizing the phase reactor of the M^3C to reduce its size and weight. The effectiveness was proven by experimental results in a downscaled motor drive system. Motor driving is a vital application as it plays an important role in industry production [14]. But for offshore wind transmission, different from driving applications, the sub-module number is high to reach a high voltage rating, and the frequencies on both AC sides are controlled to be constant, giving a fixed frequency ratio. This paper focuses on offshore wind FFTS application. In [15], a space vector modulation (SVM) based control was used on M^3C to realize wide frequency range operation. But SVM is not recommended to be used at high voltage level since the increasing number of sub-modules induces an exponential growth of the space vectors, making it time-consuming to compute and difficult to analyze. A widely used control method was developed in [16]. The concept of double $\boldsymbol{ABC-\alpha\beta 0}$ transformation was used to realize fully decoupled current control. But

This article has been accepted for publication in a future issue of this journal, but has not been fully edited. Content may change prior to final publication. Citation information: DOI 10.1109/ACCESS.2019.2932050, IEEE Access

some variables after two transformations were not DC but with a mixture of frequency components. A multi-hierarchy control strategy in ABC frame was developed for M^{3}C in [17]. However, this method would bring difficulties for small signal modelling as the variables were time-variant even at steady state. In this paper, the complicated nonlinear terms in ABC frame are isolated and transformed into DQ frame so that the model is convenient to interface with the control system and external AC systems. [18] focused on topologies and control of M^{3}C-based FFT but the sub-module voltage ripple was not considered. And in the case study, the M^{3}C was consisted of only 3 sub-modules in each arm and each sub-module had an average voltage of 60 kV. On the contrary, the proposed model in this paper considers more detailed dynamics of the sub-modules by including the capacitor voltage ripples. As will be shown by the small signal analysis, this is necessary because the modes related to capacitor voltage ripples can have poor damping and adversely affect stability. Moreover, the M^{3}C EMT model in this paper has a sub-module number of 40 and average voltage of 1.5 kV considering the IGBT capability nowadays. The mathematical model and the time-domain simulation are more realistic and accurate.

Although great effort has been spent on M^{3}C control method development, very limited attention has been paid to M^{3}C small signal modelling. The small signal model of M^{3}C should be convenient to be interlinked to different AC networks for system study. Also, as discussed earlier in this section, different control algorithms exist in the literature so the model should have easy interface with control methods. In [5], the small signal stability of an FFTS with cycloconverter was analyzed. But the AC/AC converter was modelled using only a first order time delay neglecting the dynamics from the cycloconverter and therefore the potential interaction between the converter and AC systems could not be evaluated. Contrarily, the promising AC/AC converter M^{3}C is modelled in this paper, taking into account its internal dynamics. Some work has been done on modular multilevel converter (MMC) HVDC in terms of small signal modelling [19, 20]. However, M^{3}C is fundamentally different from its multilevel counterpart. In MMC-HVDC, AC quantities are rectified to DC and transmitted until being inverted back to AC. For different needs and requirements the DC terminal can be modelled in different levels of details. In recent years, increasing attention has been paid to developing a more accurate MMC model to explore the interaction between the converter and the AC power systems or even the interaction between converters [21]. In M^{3}C, there is no DC link so quantities at two frequencies from both AC sides couple together in nine arms of the converter. Such operation is not common and therefore it is of significant importance to understand the dynamics of the M^{3}C and its impact on the power grids. However, to the best knowledge of the authors, a small signal model of M^{3}C does not exist in the literature yet. The main contribution of this paper is to develop a small signal model of the M^{3}C for FFTS which can be used for small signal dynamic studies and controller design. Besides, a small signal analysis is carried out, giving insights to system stability and parameter selection on controller and sub-module capacitors. Frequencies from both AC sides mingling in the M^{3}C are isolated and decoupled. The model is developed in DQ frame and it can be interlinked simply with the external AC systems and the control system. It is shown that the model is with a reduced number of variables but maintains satisfactory accuracy.

The rest of the paper is organized as follows. Section II introduces the operating principle of the M^{3}C for FFTS. The voltage and current equations are derived at steady state. Section III develops the small signal model of the M^{3}C for FFTS, considering the dynamics of the capacitor DC and ripple voltage components, AC current and the control system including the vector control, PLL and signal measurement. In Section IV, the developed small signal model is verified by a comparison with the time domain simulation of a detailed EMT model in RTDS. The influences of the control parameters and sub-module capacitance on small signal stability are analyzed. Section V provides a summary of the paper.

II. M^{3}C OPERATING PRINCIPLE FOR FFTS

An offshore wind FFTS is shown in Fig. 1. The offshore wind farm generates power at 20 Hz and it is transmitted at fractional frequency until the onshore M^{3}C station steps up the frequency back to the system frequency at 60 Hz.

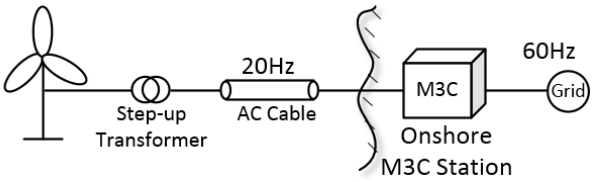

FIGURE 1. Illustrative diagram of an offshore wind FFTS.

The schematic diagram of the M^{3}C is shown in Fig. 2. It is a three-phase to three-phase AC/AC converter with a total of nine arms. The subscripts *a, b, c* represent quantities at the generator side for voltage and current while subscripts *u, v, w* represent quantities at the system side. Current direction is as shown in Fig. 2. In each of the nine arms, there are *N* IGBT based full bridge sub-modules, a resistor representing internal converter losses and an arm reactor. The performance of a system is greatly affected by the switching devices [22]. Therefore, it is important to model the switching behavior of the converter precisely. Considering a single sub-module in an arm, the switching signal $\boldsymbol{S_{armi}}$ (=1, 0, -1) determines the operation mode of the i^{th} sub-module. When the switching signal equals to 1, the sub-module is positively inserted with the capacitor voltage $\boldsymbol{u_{dc}}$. Contrarily, $-\boldsymbol{u_{dc}}$ would be inserted if the signal is -1, while the sub-module would be bypassed if the

This article has been accepted for publication in a future issue of this journal, but has not been fully edited. Content may change prior to final publication. Citation information: DOI 10.1109/ACCESS.2019.2932050, IEEE Access

signal is 0. Refer $\boldsymbol{i_{arm}}$ to the arm current and *C* is the submodule capacitance. The current equation of one sub-module and one arm can be given by (1) and (2):

$$\boldsymbol{S_{armi}\, i_{arm}} = \boldsymbol{C}\,\frac{\boldsymbol{du_{dc}}}{\boldsymbol{dt}} \tag{1}$$

$$\begin{aligned}\textstyle\sum_{i=1}^{N} \boldsymbol{S_{armi}\, i_{arm}} &= \boldsymbol{N\,C}\,\frac{\boldsymbol{du_{dc}}}{\boldsymbol{dt}} \\ \boldsymbol{n\ i_{arm}} &= \boldsymbol{N\,C}\,\frac{\boldsymbol{du_{dc}}}{\boldsymbol{dt}}\end{aligned} \tag{2}$$

Under normal operation, submodules are inserted in a same direction. Therefore, the magnitude of *n* is the inserted number of sub-modules, with *n*>0 as sub-modules positively inserted and n<0 as sub-modules negatively inserted. Define the arm switching function $\boldsymbol{S_{arm}} = n/N$, (2) becomes:

$$\boldsymbol{S_{arm}\ i_{arm}} = \boldsymbol{C}\,\frac{\boldsymbol{du_{dc}}}{\boldsymbol{dt}} \tag{3}$$

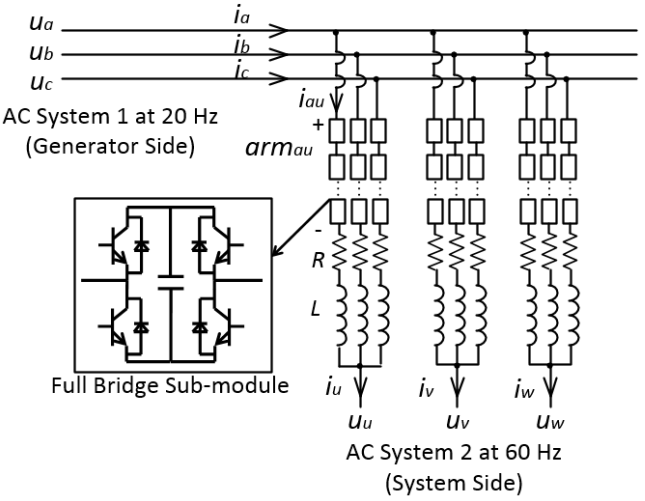

FIGURE 2. Schematic diagram of a M^{3}C.

Equation (3) gives the current relation of a M^{3}C arm, and the voltage relation can be expressed by (4), where $\boldsymbol{u_{arm}}$ represents the arm voltage:

$$\boldsymbol{u_{arm}} = \boldsymbol{N\,S_{arm}\,u_{dc}} \tag{4}$$

Within an arm, the sub-module voltage balancing method is the same for MMC-HVDC [23], which has been widely researched and tested [24]. In this study, it is assumed that the sub-modules voltage balancing control performs satisfactorily. Equations (3) and (4) assume that the sub-module voltages are balanced at steady state. The focus of this paper is to develop a compact and manageable M^{3}C small signal model. But multilevel converters for transmission applications contain up to several hundred sub-modules, making it mathematically inefficient to consider dynamics on every single sub-module for a small signal model.

Quantities with the generator side frequency (20 Hz) and those with system side frequency (60 Hz) couple in the M^{3}C. At balanced steady state, AC side current spreads equally into three arms [25]. Take arm current $\boldsymbol{i_{au}}$ for instance, it contains one third of the phase current $\boldsymbol{i_a}$ and one third of the phase current $\boldsymbol{i_u}$. Current harmonics are not taken into consideration in the model due to the reasons below: 1) By carefully select the values of circuit components, for example capacitors and inductors, the magnitudes of the current harmonics are kept to a negligible level [26, 27]. 2) The small signal model focuses on the external characteristics of the M^{3}C. For circulating currents flowing within the converter, their influence on the outer AC systems can be neglected. 3) Under AC system unbalance, current harmonics may be salient. But such situation is out of the scope of this paper. Consequently, the arm current can be expressed as:

$$\boldsymbol{i_{au}} \approx \boldsymbol{I_a\,sin(\omega_1 t + \beta_1)} + \boldsymbol{I_u\,sin(\omega_3 t + \beta_3)} \tag{5}$$

where $\boldsymbol{I_a}$, $\boldsymbol{I_u}$ $\boldsymbol{\omega_1}$, $\boldsymbol{\omega_3}$, $\boldsymbol{\beta_1}$ *and* $\boldsymbol{\beta_3}$ are the magnitudes (equaling to one third of the AC system phase currents magnitudes), angular frequencies and phase angles of the 20 Hz and 60 Hz currents in the arm. Also, the arm switching function is given by:

$$\boldsymbol{S_{au}} = \frac{\boldsymbol{E_a}}{\boldsymbol{U_{DC}}}\boldsymbol{sin(\omega_1 t + \alpha_1)} + \frac{\boldsymbol{E_u}}{\boldsymbol{U_{DC}}}\boldsymbol{sin(\omega_3 t + \alpha_3)} \tag{6}$$

where $\frac{\boldsymbol{E_a}}{\boldsymbol{U_{DC}}}$ and $\frac{\boldsymbol{E_u}}{\boldsymbol{U_{DC}}}$ are the modulation ratios at 20 Hz and 60 Hz. $\boldsymbol{E_a}$, $\boldsymbol{E_u}$, $\boldsymbol{\alpha_1}$ and $\boldsymbol{\alpha_3}$ are the magnitudes and phase angles of the modulation voltages. $\boldsymbol{U_{DC}}$ is the total arm DC voltage.

III. SMALL SIGNAL MODEL OF THE M^{3}C BASED FFTS

A. DYNAMICS OF THE CAPACITOR VOLTAGE

The ABC quantities are transformed into DQ using park's transformation. The transformation matrix is denoted as *T*:

$$T = \frac{2}{3}\begin{bmatrix} cos(\omega t) & cos(\omega t - \frac{2}{3}\pi) & cos(\omega t + \frac{2}{3}\pi) \\ -sin(\omega t) & -sin(\omega t - \frac{2}{3}\pi) & -sin(\omega t + \frac{2}{3}\pi) \end{bmatrix} \tag{7}$$

When frequency equals to 20 Hz, $\boldsymbol{\omega = \omega_1}$, and when frequency is 60 Hz, $\boldsymbol{\omega = \omega_3}$. The dynamic phasors of the quantities in DQ frame can be expressed as a function of the magnitude and the phase angle in ABC frame. For example:

$$\begin{cases} \boldsymbol{E_{d20} = E_a sin\alpha_1, E_{q20} = -E_a cos\alpha_1} \\ \boldsymbol{I_{d20} = I_a sin\beta_1, I_{q20} = -I_a cos\beta_1} \end{cases} \tag{8}$$

Substitute (5) and (6) into (3), the DC component of the capacitor voltage can be extracted and expressed as:

$$\boldsymbol{C \cdot \dot{U}_{dc\_0}} = \frac{\boldsymbol{E_a I_a}}{\boldsymbol{U_{DC}}}\boldsymbol{cos(\alpha_1 - \beta_1)} + \frac{\boldsymbol{E_u I_u}}{\boldsymbol{U_{DC}}}\boldsymbol{cos(\alpha_3 - \beta_3)} \tag{9}$$

Express the right side of (9) with DQ components and rearrange the equation, the differential equation of $\boldsymbol{U_{dc\_0}}$ can be given by:

$$\boldsymbol{\dot{U}_{dc_0}} = \frac{\boldsymbol{1}}{\boldsymbol{2U_{DC} \cdot C}}\,(\boldsymbol{E_{q20}I_{q20} + E_{d20}I_{d20} + E_{q60}I_{q60} + E_{d60}I_{d60}}) \tag{10}$$

Similarly, the 40 Hz component of the capacitor voltage (transformed into DQ) is modelled by the following (11) and (12). Detailed derivation can be found in the appendix.

$$\boldsymbol{\dot{U}_{dc\_d2} = 2\omega_1 U_{dc\_q2} - \frac{1}{2U_{DC} \cdot C}\left(E_{q20}I_{q20} - E_{d20}I_{d20}\right)} \tag{11}$$

This article has been accepted for publication in a future issue of this journal, but has not been fully edited. Content may change prior to final publication. Citation information: DOI 10.1109/ACCESS.2019.2932050, IEEE Access

$$\dot{U}_{dc\_q2} = -2\omega_1 U_{dc\_d2} + \frac{1}{2U_{DC}\cdot C}(E_{d20}I_{q20} + E_{q20}I_{d20}) \quad (12)$$

Only the 40 Hz capacitor voltage ripple is considered and higher order components are neglected in this model, as the 40 Hz component has the largest magnitude and dominates in voltage ripples. It will be further discussed and verified by the time domain simulation in Section IV. In situations where higher order voltage ripples are preferable to be included, similar approach can be applied to model ripples (at 80, 120 Hz…) easily. But in this model:

$$u_{dc} \approx U_{dc\_0} + U_{dc\_2}\, sin(2\omega_1 t + \theta_2) \quad (13)$$

B. DYNAMICS OF THE AC CURRENT

Substitute (6) and (13) into (4), the 20 Hz and 60 Hz arm voltages can be calculated as:

$$\begin{cases} U_{arm_{20a}} = \dfrac{NE_a U_{dc_0}}{U_{DC}} sin(\omega_1 t + \alpha_1) \\ \quad + \dfrac{NU_{dc\_2}E_a}{2U_{DC}} cos(\omega_1 t + \theta_2 - \alpha_1) \\ U_{arm\_60u} = \dfrac{E_u U_{dc\_0}}{U_{DC}} \sin(\omega_3 t + \alpha_3) \end{cases} \quad (14)$$

Rewriting (14) in DQ components yields:

$$\begin{cases} U_{arm\_20d} = \dfrac{NU_{dc\_0}}{U_{DC}} E_{d20} + \dfrac{N}{2U_{DC}}(U_{dc\_q2}E_{q20} + U_{dc\_d2}E_{d20}) \\ U_{arm\_20q} = \dfrac{NU_{dc\_0}}{U_{DC}} E_{q20} - \dfrac{N}{2U_{DC}}(U_{dc\_d2}E_{q20} - U_{dc\_q2}E_{d20}) \end{cases} \quad (15)$$

$$\begin{cases} U_{arm\_60d} = \dfrac{U_{dc\_0}}{U_{DC}} E_{d60} \\ U_{arm\_60q} = \dfrac{U_{dc\_0}}{U_{DC}} E_{q60} \end{cases} \quad (16)$$

Apply Kirchhoff's law to M^{3}C, equations at 20 Hz and 60 Hz can be given by:

$$\begin{cases} e_a = U_{arm\_20a} + L\cdot \dot{\imath}_{au\_20} + R\cdot i_{au\_20} \\ 0 = U_{arm\_60u} + L\cdot \dot{\imath}_{au\_60} + R\cdot i_{au\_60} + e_u \end{cases} \quad (17)$$

Again transform voltage equations into DQ coordinate. The differential equations of the AC currents are computed as:

$$\begin{cases} \dot{I}_{d20} = \frac{1}{L}U_{d20} - \frac{R}{L}I_{d20} + \omega_1 I_{q20} - \frac{1}{L}U_{arm\_20d} \\ \dot{I}_{q20} = \frac{1}{L}U_{q20} - \frac{R}{L}I_{q20} - \omega_1 I_{d20} - \frac{1}{L}U_{arm\_20q} \end{cases} \quad (18)$$

$$\begin{cases} \dot{I}_{d60} = -\frac{1}{L}U_{d60} - \frac{R}{L}I_{d60} + \omega_3 I_{q60} - \frac{1}{L}U_{arm\_60d} \\ \dot{I}_{q60} = -\frac{1}{L}U_{q60} - \frac{R}{L}I_{q60} - \omega_3 I_{d60} - \frac{1}{L}U_{arm\_60q} \end{cases} \quad (19)$$

To combine, the M^{3}C itself can be modelled with the state and input variables below:

$$x_{m3c} = [U_{dc\_0}, U_{dc\_d2}, U_{dc\_q2}, I_{d20}, I_{q20}, I_{d60}, I_{q60}]$$

$$u_{m3c} = [E_{d20}, E_{q20}, E_{d60}, E_{q60}, \omega_1, \omega_3, U_{d20}, U_{q20}, U_{d60}, U_{q60}]$$

C. CONTROL SYSTEM FOR THE M^{3}C

The control method of the M^{3}C in this study adopts the widely used vector control. Among different control methods [9, 15, 28, 29], the vector control has merits of easy implementation and satisfactory transient performance. The generator side of the M^{3}C is responsible for controlling active power and the system side of the M^{3}C is responsible for controlling capacitor voltage. The Q axis of the outer loop can be used to control voltage or reactive power. For the sake of simplicity, the Q axis current reference is given to zero to maximize the active power transmitting capability. The control diagram is as shown in Fig. 3. As the vector control algorithm has been well documented in the literature [30, 31]. The differential equations are given here directly:

$$\begin{aligned} \dot{x}_1 &= P_{20\_ref} - P_{20mea} \\ \dot{x}_2 &= k_{p1}P_{20\_ref} - k_{p1}P_{20mea} + k_{i1}x_1 - I_{d20} \\ \dot{x}_3 &= I_{q20\_ref} - I_{q20} \\ \dot{x}_4 &= U_{dc\_0} - U_{dc\_ref} \\ \dot{x}_5 &= k_{p4}U_{dc\_0} - k_{p4}U_{dc\_ref} + k_{i4}x_4 - I_{d60} \\ \dot{x}_6 &= I_{q60\_ref} - I_{q60} \end{aligned} \quad (20)$$

The PLL provides angle reference and its dynamics should be included. The modelling method is the same as proposed in [32]. Four variables are added to model two PLLs at 20 Hz and 60 Hz sides. x_7 and x_8 are the time integration of the Q axis voltages. And x_{pll} represents the output of the PLL. Its control diagram is shown in Fig. 4.

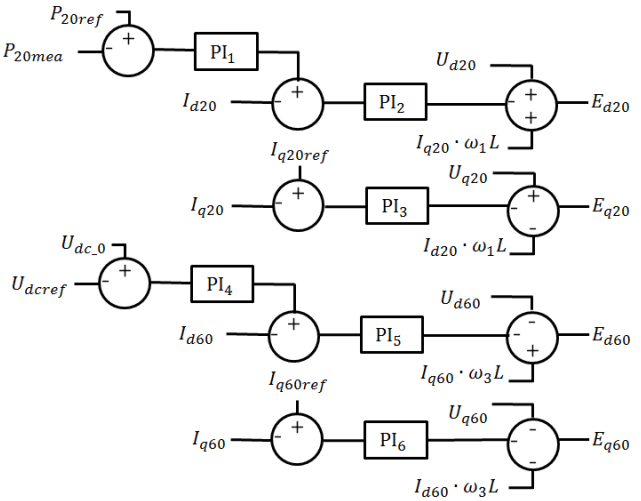

FIGURE 3. Vector control topology of the M^{3}C.

$$\begin{aligned} \dot{x}_7 &= U_{q20} \\ \dot{x}_{pll20} &= -k_{p-pll}U_{q20} - k_{i-pll}x_7 \\ \dot{x}_8 &= U_{q60} \\ \dot{x}_{pll60} &= -k_{p-pll}U_{q60} - k_{i-pll}x_8 \end{aligned} \quad (21)$$

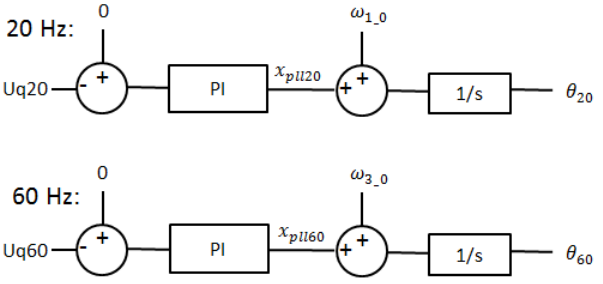

FIGURE 4. Control diagram of PLL at 20 Hz and 60 Hz.

The measurement and calculation delay is modelled by a first order low pass filter for the power signal. It also filters

This article has been accepted for publication in a future issue of this journal, but has not been fully edited. Content may change prior to final publication. Citation information: DOI 10.1109/ACCESS.2019.2932050, IEEE Access

the high frequency fluctuation. The differential equation is given by the following (22), where $\boldsymbol{P_{20}}$ is the power transmitted from the 20 Hz side, which is a function related to $\boldsymbol{U_{d20}}, \boldsymbol{I_{d20}}, \boldsymbol{U_{q20}}$ and $\boldsymbol{I_{q20}}$. $\boldsymbol{P_{20mea}}$ is the measured power at the 20 Hz side, and $\boldsymbol{T_{mea}}$ is the first order time constant.

$$\dot{\boldsymbol{P}}_{\boldsymbol{20mea}} = \frac{\boldsymbol{P_{20}}}{\boldsymbol{T_{mea}}} - \frac{\boldsymbol{P_{20mea}}}{\boldsymbol{T_{mea}}} \quad (22)$$

In total, the combined control system has the following state and input variables:

$\boldsymbol{x_{ctrl}} = [\boldsymbol{x_1}, \boldsymbol{x_2}, \boldsymbol{x_3}, \boldsymbol{x_4}, \boldsymbol{x_5}, \boldsymbol{x_6}, \boldsymbol{x_7}, \boldsymbol{x_{pll20}}, \boldsymbol{x_8}, \boldsymbol{x_{pll60}}, \boldsymbol{P_{20mea}}]$

$u_{ctrl} = [U_{dc\_0}, I_{d20}, I_{q20}, I_{d60}, I_{q60}, U_{d20}, U_{q20}, U_{d60}, U_{q60}, P_{20ref}, I_{q20ref}, U_{dcref}, I_{q60ref}]$

D. COMBINED SMALL SIGNAL MODEL

To get the small signal model of the complete system, the abovementioned two systems: the M^{3}C system and its control system are merged. In the first system, $E_{d20}, E_{q20}, E_{d60}$ and E_{q60} are the outputs from the vector control in the second system. And ω_1 and ω_3 are the outputs from the PLLs. $U_{d20}, U_{q20}, U_{d60}$ and U_{q60} provide interfaces with the 20 Hz and 60 Hz side AC systems respectively. The combined model can be expressed in the form of:

$$\dot{x} = Ax + Bu \quad (23)$$

where the expression of the matrix A and B is given in the appendix. The small signal model can be derived by linearizing (23). The final model is of 18th order and all variables are listed below:

$\Delta\boldsymbol{x} = [\Delta\boldsymbol{U_{dc\_0}}, \Delta\boldsymbol{U_{dc\_d2}}, \Delta\boldsymbol{U_{dc\_q2}}, \Delta\boldsymbol{I_{d20}}, \Delta\boldsymbol{I_{q20}}, \Delta\boldsymbol{I_{d60}}, \Delta\boldsymbol{I_{q60}}, \Delta\boldsymbol{x_1}, \Delta\boldsymbol{x_2}, \Delta\boldsymbol{x_3}, \Delta\boldsymbol{x_4}, \Delta\boldsymbol{x_5}, \Delta\boldsymbol{x_6}, \Delta\boldsymbol{x_7}, \Delta\boldsymbol{x_{pll20}}, \Delta\boldsymbol{x_8}, \Delta\boldsymbol{x_{pll60}}, \Delta\boldsymbol{P_{20mea}}]$

$\Delta u = [\Delta U_{d20}, \Delta U_{q20}, \Delta U_{d60}, \Delta U_{q60}, \Delta P_{20ref}, \Delta I_{q20ref}, \Delta U_{dcref}, \Delta I_{q60ref}]$

IV. MODEL VERIFICATION AND STABILITY ANALYSIS

To validate the proposed small signal model, the combined model discussed in Section III is implemented in MATLAB/Simulink. Also, a non-linear detailed model of M^{3}C is developed in RTDS for EMT simulation. For the EMT model, a small simulation time step of 3 μs is adopted to precisely simulate the switching dynamics of the power electronics. Unlike most existing research in the literature where only several sub-modules are considered in each arm, this model contains as many as 40 sub-modules in each arm for all 9 arms in the M^{3}C, presenting an accurate representation of the AC/AC multilevel converter. The simulated system topology is as shown in Fig. 2 with the AC system modelled as a voltage source behind a Thevenin impedance. For the IGBT switches, the build-in module in RTDS is used. Implementation of IGBT-based switches modelling in RTDS for modular multilevel converters is described in [33], with more technical details in [34]. The 'MMC5' model is adopted since for small signal study, the exact firing pulse for each individual sub-module is not concerned. The control system was developed according to the control diagram Fig. 3. Full details of the system parameters can be found in Table I in the appendix. In this section, firstly the performance of M^{3}C as the frequency changer is shown to be satisfactory by ideal voltage and current profiles. And then the dynamic responses of a step change between the small signal model and the time domain EMT model are compared. The comparison shows that the proposed model is of high accuracy. Next, small signal analysis is carried out on control parameters. The results from eigenvalue analysis precisely match the results from frequency domain analysis, and can be verified by time domain simulation. Again the correctness of the small signal model is validated. Also, analysis is given on the influence of sub-module capacitance on the small signal stability.

In time domain simulation, Fig. 5 (a) and (b) show the sinusoidal voltage and current waveforms at the 20 Hz and 60 Hz AC sides. The arm voltages and currents are shown in Fig. 5 (c), which are regular superposition waveforms of 20 Hz and 60 Hz sinusoidal components as discussed in Section II. The arm voltage ripple and current ripple are small at only 0.096% and 1.59% respectively. It is shown that M^{3}C performs well as the AC/AC converter and it has the advantage of low ripple level. In RTDS, The actual measured sub-module voltage is plotted in Fig. 6, together with the sub-module voltage added up only by the DC component and 40 Hz ripple. It can be seen from the figure that the 40 Hz component takes up the largest magnitude of the ripples and two curves match closely. The dominant ripple at 40 Hz has a magnitude of 0.05 kV or 3.33% of the DC component. High order ripples have negligible amounts that are less than 1%. Thus, the discrepancy brought by neglecting high order capacitor voltage ripples is acceptable. If required, the proposed approach is capable of modelling high order ripple components.

A. DYNAMIC RESPONSE OF STEP CHANGE ON ACTIVE POWER REFERENCE

At initial state, 30 MW of active power is transmitted from the 20 Hz side to the 60 Hz side. At t = 0.4s, a step change of $\boldsymbol{P_{20ref}}$ is applied from 30 MW to 32 MW. The dynamic

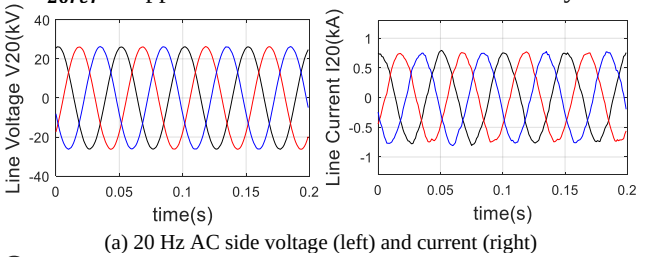

(a) 20 Hz AC side voltage (left) and current (right)

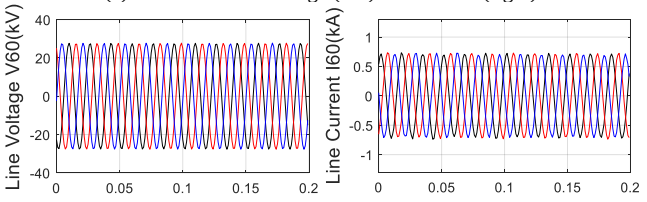

(b) 60 Hz side AC voltage (left) and current (right)

This article has been accepted for publication in a future issue of this journal, but has not been fully edited. Content may change prior to final publication. Citation information: DOI 10.1109/ACCESS.2019.2932050, IEEE Access

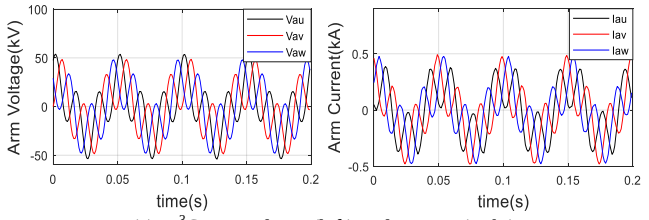

(c) M^3C arm voltage (left) and current (right)

FIGURE 5. Voltage and current waveforms in simulation.

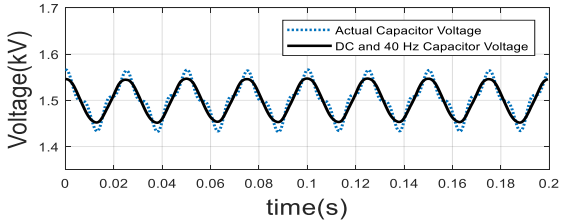

FIGURE 6. Measured sub-module capacitor voltage and capacitor voltage with only DC component and 40 Hz ripple.

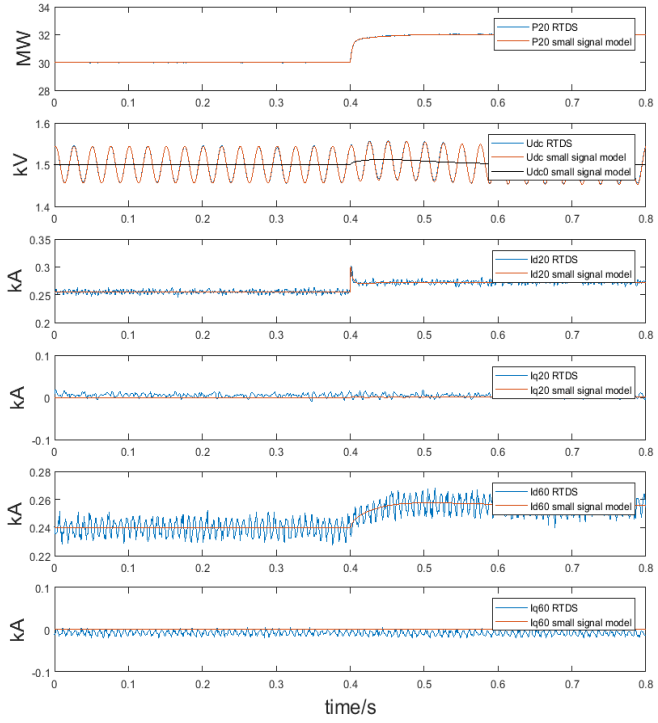

FIGURE 7. Step change response of the small signal model (red line) and detailed EMT model (blue line). From up to down: 1) measured active power at 20 Hz side, 2) capacitor voltage (DC+40 Hz superposition), 3-4) D/Q axis current 20 Hz side, 5-6) D/Q axis current 60 Hz side.

response of the developed small signal model is compared with the detailed time domain simulation. As can be seen in Fig. 7, the active power at 20 Hz side and the capacitor voltage show great consistency. For AC current waveforms, overall there is good agreement, except that the detailed simulation model contains minor high frequency fluctuations. Step change dynamic response validates the small signal model.

B. INFLUENCE OF THE OUTER LOOP CONTROLLER

The developed small signal model is helpful on the selection of controller parameters. In this sub-section, the outer loop PI controller parameter $\boldsymbol{k_{i1}}$ is studied. The root locus of the related modes is plotted in Fig. 8. As $\boldsymbol{k_{i1}}$ increases, the eigenvalues move towards the right half of the complex plane and the modes finally become unstable. In RTDS, a step change of $\boldsymbol{k_{i1}}$ from 15 to 150 is applied at t=0.25s. Since this controller is responsible for controlling the active power at the 20 Hz side, the waveform of the measured $\boldsymbol{P_{20}}$ is shown in Fig. 9. As can be seen, the system loses stability and the active power begins to oscillate with a period of 0.0047s. According to the eigenvalue analysis, the oscillation period of this mode is calculated as $\boldsymbol{2\pi/\omega}$ = 0.0048s, which agrees with the simulation result. Also in frequency domain, the bode plots are shown as Fig. 10 when $\boldsymbol{k_{i1}}$ is small and Fig. 11 when $\boldsymbol{k_{i1}}$ is large, with the input as the active power reference and the output as the measured active power at the 20 Hz side. As can be seen, when $\boldsymbol{k_{i1}}$ is small, the system is stable, while when $\boldsymbol{k_{i1}}$ is large, a resonant point is spotted at 208 Hz, which exactly matches the eigenvalue analysis (1/0.0048s≈208 Hz) and the time domain simulation. The effectiveness of the proposed model is again validated. It is shown that the increasing outer loop integral gain has a negative effect on the small signal stability and therefore should be limited within a certain range.

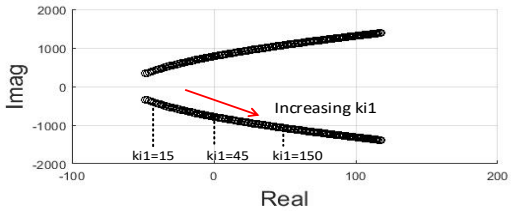

FIGURE 8. Root locus of the eigenvalues when ki1 increases.

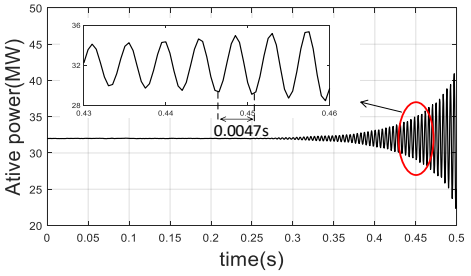

FIGURE 9. Active power at 20 Hz side when step change is applied to ki1.

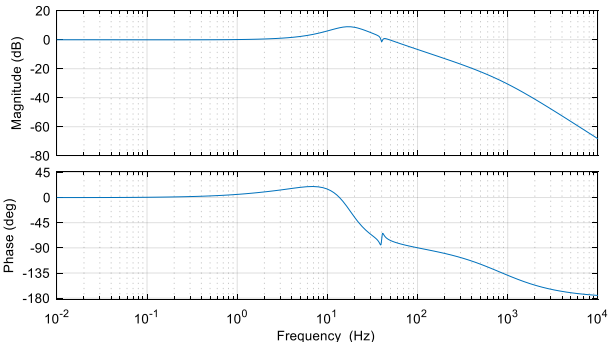

This article has been accepted for publication in a future issue of this journal, but has not been fully edited. Content may change prior to final publication. Citation information: DOI 10.1109/ACCESS.2019.2932050, IEEE Access

FIGURE 10. Frequency response when ki1 is 15 (stable).

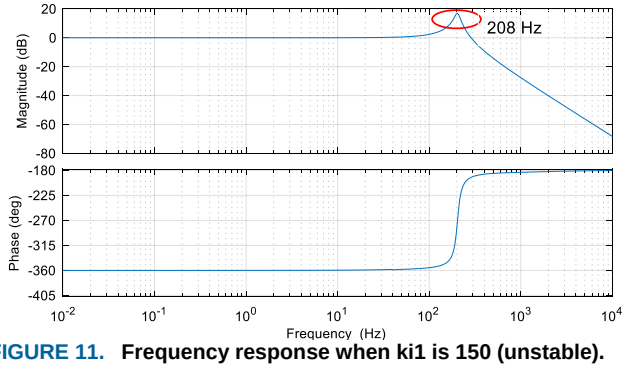

FIGURE 11. Frequency response when ki1 is 150 (unstable).

C. INFLUENCE OF THE PLL

In this sub-section, the control parameters of the PLL are analyzed. If the eigenvalue of a mode is denoted as $\lambda = \sigma \pm j\omega$, the damping ratio of the mode is defined as $\xi = -\sigma/\sqrt{\sigma^2 + \omega^2}$. When the damping ratio is less than 5%, the mode is regarded as poorly damped. Fig. 12 plots the damping ratio of the mode related to PLL as the proportional gain grows from 0 to 2. It is shown that the damping ratio increases and then remains at 1. This mode has poor damping when k_{ppll}<0.06. In addition, the root locus is plotted in Fig. 13 when k_{ppll} varies from 0-20 and k_{ipll} varies from 1-20. When k_{ppll} raises, the eigenvalues firstly move towards and then get onto the real axis. After that, one eigenvalue moves further away from the imaginary axis while the other gets closer to the right half pane. As a result, if k_{ppll} adopts a large value, the system may be vulnerable to small signal instability. For the integral gain, the mode trajectory is more straightforward. As k_{ipll} increases, the eigenvalue gets more negative and therefore the small signal stability enhances. To sum up, the selection of k_{ppll} should be careful as it cannot be too small or too large. While a large k_{ipll} is preferred since that would bring more damping to the mode.

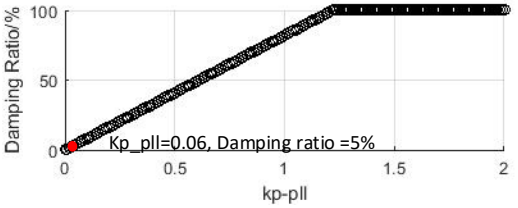

FIGURE12. Damping ratio as PLL proportional gain grows.

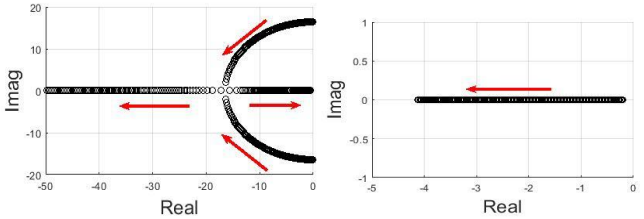

FIGURE13. Root locus when k_ppll (left) and k_ipll (right) increase.

D. ANALYSIS OF THE SUB-MODULE CAPACITOR MODE

The small signal stability of the mode related to the capacitor voltage ripple is analyzed in this subsection. The damping ratio is plotted against the sub-module capacitance in Fig. 14.

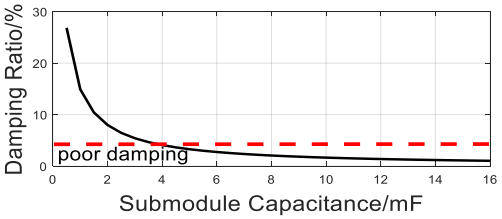

FIGURE14. Damping ratio of the mode related to capacitor ripple as sub-module capacitance increases.

As can be seen, a larger value of the capacitor would result in poorer damping of the mode. In other small signal studies for instance for two-level VSC or MMC, capacitor ripples are often omitted and it is assumed that the capacitor voltage is DC [35]. However, the M^{3}C model proposed in this paper takes into account the sub-module voltage ripples. Therefore, it is able to analyze the possible poorly damped mode and the small signal analysis can help select the sub-module capacitance. It is found that including capacitor voltage ripple in the small signal modelling is necessary as their modes can have poor damping and affect the small signal stability of the system. Based on the results in this case, the sub-module capacitance should not be larger than 4 mF to avoid poor damping.

V. CONCLUSION

As M^{3}C based FFTS is a promising solution for offshore wind power integration, there is need of a model to study its influence on the existing power systems. The basic achievements of this paper are to develop a small signal model of M^{3}C and to conduct a small signal analysis giving insights to system stability and parameter selection. The model provides easy interfaces with both the external AC systems and the control system. In the model, the dynamics of AC currents and the DC and ripple components on sub-module capacitor voltage have been considered. The control system has included dynamics of the outer and inner loop PI controllers, PLL and measurement delay. According to the small signal analysis, it has been found that increasing the integral gain of the D axis outer loop control has an adverse effect and can induce power oscillation, while a larger integral gain of the PLL improves the small signal stability. The choice of the proportional gain of the PLL should be within a certain range as the damping ratio can be poor when a very small gain is chosen but a very large gain would result in poor damping. Also, the damping ratio of the capacitor ripple voltage mode decreases as capacitance grows.

The performance of the proposed model is satisfactory. Based on the comparison between the detailed EMT M^{3}C model and the small signal model, a very good matching on both dynamic response and stability analysis has been shown, validating the accuracy of the proposed model. The

This article has been accepted for publication in a future issue of this journal, but has not been fully edited. Content may change prior to final publication. Citation information: DOI 10.1109/ACCESS.2019.2932050, IEEE Access

assumption of balanced sub-converters and the discrepancy brought by neglecting high order sub-module voltage ripples have been analyzed by the time domain simulation. For future work, the proposed model can be enhanced by considering unbalanced operating conditions and system harmonics resonances. Also, it would be beneficial to develop a prototype of M^3C and carry out field tests.

APPENDIX

A. DETAILED DERIVATION OF THE SMALL SIGNAL MODEL

The full Kirchhoff's law equations can be expressed as:

$$\begin{bmatrix} u_a & u_a & u_a \\ u_b & u_b & u_b \\ u_c & u_c & u_c \end{bmatrix} = \begin{bmatrix} v_{au} & v_{av} & v_{aw} \\ v_{bu} & v_{bv} & v_{bw} \\ v_{cu} & v_{cv} & v_{cw} \end{bmatrix} + \left(R + L\frac{d}{dt}\right)\begin{bmatrix} i_{au} & i_{av} & i_{aw} \\ i_{bu} & i_{bv} & i_{bw} \\ i_{cu} & i_{cv} & i_{cw} \end{bmatrix} + \begin{bmatrix} u_u & u_v & u_w \\ u_u & u_v & u_w \\ u_u & u_v & u_w \end{bmatrix} \quad \begin{matrix} (A1-A3) \\ (A4-A6) \\ (A7-A9) \end{matrix}$$

Apply $ABC-\alpha\beta 0$ transformation to A1-A3, A4-A6, and A7-A9 respectively and extract the zero sequence equations:

$$\begin{bmatrix} u_a \\ u_b \\ u_c \end{bmatrix} = \begin{bmatrix} v_{a0} \\ v_{b0} \\ v_{c0} \end{bmatrix} + \left(R + L\frac{d}{dt}\right)\begin{bmatrix} i_{a0} \\ i_{b0} \\ i_{c0} \end{bmatrix} + \begin{bmatrix} u_{060} \\ u_{060} \\ u_{060} \end{bmatrix} \quad \begin{matrix} (A10) \\ (A11) \\ (A12) \end{matrix}$$

When the AC system is balanced, there is no zero sequence voltage so u_{060} can be omitted. Further apply $ABC-DQ$ transformation to A10-A12:

$$\begin{bmatrix} E_{d20} \\ E_{q20} \end{bmatrix} = \begin{bmatrix} U_{d20} \\ U_{q20} \end{bmatrix} - \left(R + L\frac{d}{dt}\right)\begin{bmatrix} I_{d20} \\ I_{q20} \end{bmatrix} + \omega_1 L\begin{bmatrix} I_{q20} \\ -I_{d20} \end{bmatrix} \quad \begin{matrix} (A13) \\ (A14) \end{matrix}$$

where E_{d20} and E_{q20} are the DQ arm voltage for 20 Hz. In this form, decoupled control can be applied to form the inner current loop. The outer loop at 20 Hz is selected to control active power. The 60 Hz side can be derived using similar approach. Or alternatively, after the $ABC-\alpha\beta 0$ transformation, apply Park's transformation to three sets of equations in $\alpha\beta$ frame. At symmetrical state, the cluster voltages are balanced [28], so V_{adq}, V_{bdq} and V_{cdq} can be denoted as E_{d60} and E_{q60} uniformly:

$$\begin{bmatrix} E_{d60} \\ E_{q60} \end{bmatrix} = -\begin{bmatrix} U_{d60} \\ U_{q60} \end{bmatrix} - \left(R + L\frac{d}{dt}\right)\begin{bmatrix} I_{d60} \\ I_{q60} \end{bmatrix} + \omega_3 L\begin{bmatrix} I_{q60} \\ -I_{d60} \end{bmatrix} \quad \begin{matrix} (A15) \\ (A16) \end{matrix}$$

Outer loop is selected to balance the capacitor voltage of three clusters respectively. Take cluster A for instance, the differential equation of the 40 Hz capacitor voltage ripple can be calculated as:

$$C\dot{U}_{dc\_a2} = -\frac{E_a I_a}{2U_{DC}}\cos(2\omega_1 + \alpha_1 + \beta_1) \qquad (A17)$$

Transform the equation into DQ frame, (11) and (12) in Section III can be derived.

B. CIRCUIT AND CONTROL PARAMETERS

TABLE I

Symbol	Quantity	Value
f_1	Fractional frequency	20 Hz
f_3	System frequency	60 Hz
V_{l-l}	Rated AC system voltage	33 kV
N	Sub-module number each arm	40
L	Inductance	15 mL
C	Sub-module capacitance	5 mF
R	Arm resistance	0.25 Ω
U_{dcref}	Capacitor voltage reference	1.5 kV
P_{20ref}	Active power reference 20 Hz	30 MW
I_{qref}	Q axis current reference	0 kA
k_{p1}, k_{i1}	PI controller 1 parameters	0.025, 1
k_{p2}, k_{i2}	PI controller 2 parameters	100, 20
k_{p3}, k_{i3}	PI controller 3 parameters	100, 20
k_{p4}, k_{i4}	PI controller 4 parameters	0.5, 10
k_{p5}, k_{i5}	PI controller 5 parameters	50, 50
k_{p6}, k_{i6}	PI controller 6 parameters	50, 50
k_{ppll}, k_{ipll}	PLL parameters	5, 100
T_{mea}	First order time constant of measurement	0.01s

C. EXPRESSION OF STATE SPACE MODEL MATRICES

Please see below (Left: A matrix; Right: B matrix).

$$\begin{bmatrix}
 & & & \frac{E_{d20}}{2U_{DC}\cdot C} & \frac{E_{q20}}{2U_{DC}\cdot C} & \frac{E_{d60}}{2U_{DC}\cdot C} & \frac{E_{q60}}{2U_{DC}\cdot C} \\
 & & 2\omega_1 & \frac{E_{q20}}{2U_{DC}\cdot C} & -\frac{E_{d20}}{2U_{DC}\cdot C} & & \\
 & -2\omega_1 & & \frac{E_{q20}}{2U_{DC}\cdot C} & \frac{E_{d20}}{2U_{DC}\cdot C} & & \\
-\frac{NE_{d20}}{LU_{DC}} & -\frac{NE_{d20}}{2LU_{DC}} & -\frac{NE_{q20}}{2LU_{DC}} & -\frac{R}{L} & \omega_1 & & \\
-\frac{NE_{q20}}{LU_{DC}} & \frac{NE_{q20}}{2LU_{DC}} & -\frac{NE_{d20}}{2LU_{DC}} & -\omega_1 & -\frac{R}{L} & & \\
-\frac{NE_{d60}}{LU_{DC}} & & & & & -\frac{R}{L} & \omega_3 \\
-\frac{NE_{q60}}{LU_{DC}} & & & & & -\omega_3 & -\frac{R}{L} \\
 & & & -1 & & & & k_{i1} \\
 & & & & -1 & & & \\
1 & & & & & & & \\
k_{p4} & & & & & -1 & & & k_{i4} \\
 & & & & & & -1 & & \\
 & & & & & & & & & -k_{i-pll} \\
 & & & & & & & & & & -k_{i-pll} \\
 & & & \frac{9U_{d20}}{2T_{fil}} & \frac{9U_{q20}}{2T_{fil}} & & & & & & & -\frac{1}{T_{mea}}
\end{bmatrix}$$

$$\begin{bmatrix}
-1 \\
-k_{p1} \\
 \\
 \\

REFERENCES

[1] Wind Europe, "Offshore Wind in Europe: Key Trends and Statistics 2018," 2018.

[2] CIGRE B4-39 Working Group, "Integration of large scale wind generation using HVDC and power electronics," *Paris: Cigre*, 2009.

[3] X. Wang, "The fractional frequency transmission system," in *Proc. IEEE 5th Annu. Conf. Jpn. Power Energy, Tokyo, Japan*, 1994, pp. 53-58.

[4] X. Xiang, M. Merlin, and T. Green, "Cost analysis and comparison of HVAC, LFAC and HVDC for offshore wind power connection," in *12th IET Int. Conf. AC DC Power Transmission*, 2016, pp. 1-6.

[5] J. Li and X. P. Zhang, "Small signal stability of fractional frequency transmission system with offshore wind farms," *IEEE Trans. on Sustainable Energy*, vol. 7, no. 4, pp. 1538-1546, 2016.

[6] J. Ruddy, R. Meere, and T. O'Donnell, "Low frequency AC transmission for offshore wind power: A review," *Renewable and Sustainable Energy Reviews*, vol. 56, pp. 75-86, 2016.

[7] S. Liu, *et al.*, "A decoupled control strategy of modular multilevel matrix converter for fractional frequency transmission system," *IEEE Trans. on Power Delivery*, vol. 32, no. 4, pp. 2111-2121, 2017.

[8] R. W. Erickson and O. A. Al-Naseem, "A new family of matrix converters," in *The 27th Annual Conf. of the IEEE*, 2001, vol. 2, pp. 1515-1520.

[9] S. Liu, M. Saeedifard, and X. Wang, "Analysis and control of the modular multilevel matrix converter under unbalanced grid conditions," *IEEE Journal of Emerging and Selected Topics in Power Electronics*, 2018.

[10] Y. Miura, *et al.*, "Modular multilevel matrix converter for low frequency AC transmission," in *IEEE 10th Int. Conf. on Power Electronics and Drive Systems* 2013, pp. 1079-1084.

[11] W. Kawamura, M. Hagiwara, and H. Akagi, "Control and experiment of a modular multilevel cascade converter based on triple-star bridge cells," *IEEE Trans. on Industry Applications*, vol. 50, no. 5, pp. 3536-3548, 2014.

[12] W. Kawamura, *et al.*, "AC-Inductors design for a modular multilevel TSBC converter, and performance of a low-speed high-torque motor drive using the converter," *IEEE Trans. on Industry Applications*, vol. 53, no. 5, pp. 4718-4729, 2017.

[13] Q. Xu, *et al.*, "Analysis and control of M3C-based UPQC for power quality improvement in medium/high-voltage power grid," *IEEE Trans. on Power Electronics*, vol. 31, no. 12, pp. 8182-8194, 2016.

[14] X. Chang and Y. Wang, "Peak-to-Peak Filtering for Networked Nonlinear DC Motor Systems With Quantization," *IEEE Trans. on Industrial Informatics*, vol. 14, no. 12, pp. 5378-5388, 2018.

[15] Y. Miura, *et al.*, "Control scheme of the modular multilevel matrix converter using space vector modulation for wide frequency range operation," in *2017 IEEE Energy Conversion Congress and Exposition (ECCE)*, 2017, pp. 1084-1091.

[16] F. Kammerer, J. Kolb, and M. Braun, "Fully decoupled current control and energy balancing of the modular multilevel matrix converter," in *15th International Power Electronics and Motion Control Conference* 2012, pp. LS2a. 3-1 - 3-8.

[17] Z. Ou and G. Wang, "Multi-hierarchy control strategy in abc coordinate for modular multilevel matrix converter in fractional frequency transmission system," *The Journal of Engineering*, vol. 2019, no. 16, pp. 1886-1891, 2019.

[18] C. Yuan, R. Zhou, and M. Tong, "Topologies and control of low-frequency alternating current for offshore wind farms based on modular multilevel matrix converter," *The Journal of Engineering*, vol. 2019, no. 16, pp. 2271-2277, 2019.

[19] A. Jamshidifar and D. Jovcic, "Small-Signal Dynamic DQ Model of Modular Multilevel Converter for System Studies," *IEEE Trans. on Power Delivery*, vol. 31, no. 1, pp. 191-199, 2016.

[20] T. Li, A. M. Gole, and C. Zhao, "Harmonic instability in MMC-HVDC converters resulting from internal dynamics," *IEEE Trans. on Power Delivery*, vol. 31, no. 4, pp. 1738-1747, 2016.

[21] N. Trinh, *et al.*, "Generic Model of MMC-VSC-HVDC for Interaction Study With AC Power System," *IEEE Transactions on Power Systems*, vol. 31, no. 1, pp. 27-34, 2016.

[22] X. Huo, *et al.*, "Observer-Based Fuzzy Adaptive Stabilization of Uncertain Switched Stochastic Nonlinear Systems with Input Quantization," *Journal of the Franklin Institute*, 2019.

[23] Q. Tu, Z. Xu, and L. Xu, "Reduced switching-frequency modulation and circulating current suppression for modular multilevel converters," *IEEE Trans. on Power Delivery*, vol. 26, no. 3, pp. 2009-2017, 2011.

[24] F. Deng and Z. Chen, "A Control Method for Voltage Balancing in Modular Multilevel Converters," *IEEE Trans. on Power Electronics*, vol. 29, no. 1, pp. 66-76, 2014.

[25] J. Ma, *et al.*, "Modular multilevel matrix converter for offshore low frequency AC transmission system," in *IEEE 26th Int. Symposium on Industrial Electronics*, 2017, pp. 768-774.

[26] Y. Tang, *et al.*, "Capacitor Selection for Modular Multilevel Converter," *IEEE Trans. on Industry Applications*, vol. 52, no. 4, pp. 3279-3293, 2016.

[27] M. Zygmanowski, B. Grzesik, and R. Nalepa, "Capacitance and inductance selection of the modular multilevel converter," in *15th European Conf. on Power Electronics and Applications (EPE)*, 2013, pp. 1-10.

[28] S. Shang, *et al.*, "Research on modeling and control strategy of modular multilevel matrix converter supplying passive networks," in *IEEE PES Asia-Pacific Power and Energy Engineering Conf.(APPEEC)*, 2016, pp. 1974-1978.

[29] X. Chang, R. Liu, and J. H. Park, "A Further Study on Output Feedback H ∞ Control for Discrete-Time Systems," *IEEE Trans. on Circuits and Systems II: Express Briefs*, 2019.

[30] F. Wu, *et al.*, "Small signal stability analysis and optimal control of a wind turbine with doubly fed induction generator," *IET Generation, Transmission & Distribution*, vol. 1, no. 5, pp. 751-760, 2007.

[31] C. Schauder and H. Mehta, "Vector analysis and control of advanced static VAr compensators," *IEE Proc. C - Generation, Transmission and Distribution*, vol. 140, no. 4, pp. 299-306, 1993.

[32] J. Z. Zhou, *et al.*, "Impact of Short-Circuit Ratio and Phase-Locked-Loop Parameters on the Small-Signal Behavior of a VSC-HVDC Converter," *IEEE Trans. on Power Delivery*, vol. 29, no. 5, pp. 2287-2296, 2014.

[33] RTDS. (2015). *MMC Modelling*. Available: https://www.rtds.com/wp-content/uploads/2015/12/MMC-Modelling-NC-170202-1.pdf

[34] K. Ou, *et al.*, "Research and application of small time-step simulation for MMC VSC-HVDC in RTDS," in *2014 International Conference on Power System Technology*, 2014, pp. 877-882.

[35] G. O. Kalcon, *et al.*, "Small-Signal Stability Analysis of Multi-Terminal VSC-Based DC Transmission Systems," *IEEE Trans. on Power Systems*, vol. 27, no. 4, pp. 1818-1830, 2012.

JIAJIE LUO received his B.Eng. degrees from the Huazhong University of Science and Technology, Wuhan, China and the University of Birmingham, Birmingham, U.K., in 2015. He is a Ph.D. candidate with the University of Birmingham. His research interests include renewable energy integration, modeling and control. He is currently working for Siemens Gamesa at its Power Converter Competence Center, UK.

This article has been accepted for publication in a future issue of this journal, but has not been fully edited. Content may change prior to final publication. Citation information: DOI 10.1109/ACCESS.2019.2932050, IEEE Access

XIAO-PING ZHANG (M'95–SM'06) is currently a Professor of electrical power systems with the University of Birmingham, U.K., and he is also the Director of Smart Grid, Birmingham Energy Institute and the Co-Director of the Birmingham Energy Storage Center. He has co-authored the first and second edition of the monograph Flexible AC Transmission Systems: Modeling and Control, (Springer in 2006 and 2012). He has co-authored the book Restructured Electric Power Systems: Analysis of Electricity Markets with Equilibrium Models, (IEEE Press/Wiley in 2010).

YING XUE received the B.Eng. degree in electrical engineering from the Huazhong University of Science and Technology (HUST), Wuhan, China, and the University of Birmingham, Birmingham, U.K., in 2012, and the Ph.D. degree in electrical engineering from the University of Birmingham, in 2016. He is a Lecturer with the University of Birmingham. His main research area is HVDC modeling and control.